Construction and Building Materials 317 (2022) 125840

Contents lists available at ScienceDirect

Construction and Building Materials

journal homepage: www.elsevier.com/locate/conbuildmat

# Micromechanics-integrated machine learning approaches to predict the mechanical behaviors of concrete containing crushed clay brick aggregates

Hyeong-Ki Kim [a], Yeonggyu Lim [b], Million Tafesse [c], G.M. Kim [d], Beomjoo Yang [b,*]

[a] Department of Architectural Engineering, Chosun University, Pilmun-daero 309, Dong-gu, Gwangju 61452, Republic of Korea
[b] School of Civil Engineering, Chungbuk National University, Chungdae-ro 1, Seowon-gu, Cheongju, Chungbuk 28644, Republic of Korea
[c] Research and Development Division, MC-Bauchemie Manufacturing Plc, Addis Ababa 5452, Ethiopia
[d] Korea Institute of Geoscience and Mineral Resources, 124 Gwahak-ro, Yuseong-gu, Daejeon 34132, Republic of Korea

ARTICLE INFO

*Keywords:*
Crushed clay brick
Young's modulus
Concrete
Micromechanics
Machine learning model

ABSTRACT

In this paper, we present micromechanics-integrated machine learning studies of concrete containing crushed clay brick as a coarse aggregate. Initially, the stress-strain responses of normal and crushed clay brick aggregates were quantitatively measured. Concrete specimens with various water/cement ratios and replacement rates of the aggregate were then fabricated and their stress-strain responses were evaluated. Concrete mixed with crushed clay brick aggregate showed lower compressive strength compared to concrete containing normal aggregate, and it was difficult to predict the material performance based on existing specifications and models. Based on results from an experimental assessment, micromechanics-integrated machine learning approaches that can effectively predict the properties of concrete mixed with crushed clay brick aggregates was developed. Several parametric studies and comparisons are carried out to verify the potential capacity of the proposed model framework.

## 1. Introduction

The construction field uses more concrete than any other material, and coarse aggregate is a significant element that forms most of the volume of concrete [1,2]. In general, the coarse aggregate is evenly distributed throughout the earth, meaning that there is no difficulty with regard to supply and demand. However, in areas where this is not the case, the construction of buildings and other infrastructure elements is significantly disrupted [3]. It is particularly difficult to obtain the coarse aggregate on islands or in desert areas, and much cost is required unnecessarily when transporting the aggregate to other regions. As a result, the need for research to develop artificial aggregates as replacements for the natural aggregates utilized in concrete is increasing [4].

Roh et al. [5] analyzed the environmental impact of concrete mixed with a by-product aggregate material by means of life cycle assessments. When bottom-ash-based artificial aggregate is applied to concrete production, the environmental cost was found to decrease by 0.9 USD/m3. In addition, Roh et al. [5] revealed that various environmental indicators have deteriorated due to the use of artificial aggregates. Castillo et al. [6] fabricated lightweight concrete specimens containing plastic waste aggregates (80% polyolefins and 20% other). Their study [6] found that the use of artificial aggregates reduced both the density and compressive strength, while increasing the ductility and the flexural strength. The addition of plastic waste aggregates also tended to deteriorate the workability of fresh mixtures. Overall, plastic waste aggregates are expected to contribute to a circular economy, but it needs to be improved. In Bangladesh, where it is difficult to extract coarse aggregates from nature, crushed brick chip made by baking red clay is used as a substitute for coarse aggregate (Fig. 1) [7]. In general, when clay is mixed with concrete, drying shrinkage increases and microcracks readily occur. Therefore, it is recommended to wash coarse aggregates with water before use to remove the clay component. Despite these non-ideal conditions, geopolitical and economical limitations have led to the use of crushed clay brick (CCB) aggregates.

Zheng et al. [8] prepared concrete containing CCB aggregates and measured the resulting compressive strength. The 28-day compressive strength of concrete containing CCB aggregates dropped 7–13%, and the reduction rate varied with the water/cement (w/c) ratio [8]. Zhao et al. [9] performed various experiments and analyzed lightweight concrete to which waste clay brick (WCB) aggregate was applied. As a result, concrete mixed with WCB aggregate was found to have a compressive strength of 40 MPa and density of 1850 kg/m$^3$. In addition, the WCB

* Corresponding author.
*E-mail address:* byang@cbnu.ac.kr (B. Yang).

https://doi.org/10.1016/j.conbuildmat.2021.125840
Received 17 August 2021; Received in revised form 15 November 2021; Accepted 23 November 2021

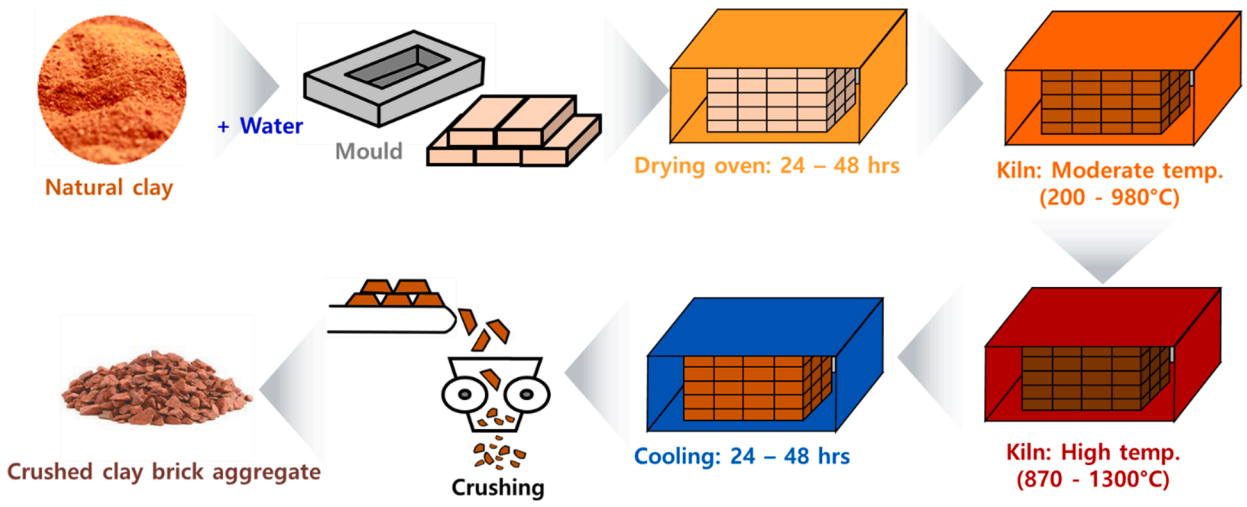


**Fig. 1.** Manufacturing process of the CCB aggregate.

mixed concrete showed excellent resistance to the freeze-thaw conditions, carbonation, and chloride penetration [9]. Pongsopha et al. [10] utilized burnt clay aggregate (BCA) as a phase-change material (PCM) carrier to increase the thermal properties of concrete. It was observed in their study [10] that BCA has the potential to be used as an effective PCM to reduce the temperature change rate of concrete. Specifically, paraffin-impregnated BCA (PIA) improved the compressive and flexural strength of concrete as well as its thermal insulation properties [10]. According to the literatures, the mechanical behavior of concrete using CCB aggregates is very different from that of general concrete. Furthermore, most of the earlier work in this area was limited to experimental investigations, and studies involving computational analyses and model establishment are very rare.

Hence, the present study experimentally and theoretically investigates concrete with CCB aggregates, examining the effects of artificial aggregate replacement and the w/c ratio. First, normal and CCB aggregates were produced as cubic-shaped specimens for stress-strain response evaluations under compressive loading. The mechanical properties of the aggregates were then applied to the proposed model for more accurate predictions. Then, concrete specimens with various CCB aggregates contents and w/c ratios were fabricated by a mixing process and their compressive behaviors were measured. In addition, a micromechanics-based constitutive equation that accounts for the various types of aggregates and for microcrack damage was derived. The derived micromechanical model was implemented to a finite element (FE) code to reproduce the experimental conditions. In the derived micromechanical model, there are model constants related to microdamage that are difficult to measure experimentally. Optimal model constants were estimated using a machine learning (ML)-based genetic algorithm (GA) and experimental data. A series of numerical studies were conducted to assess the influence of the model constants on the mechanical properties of the concrete specimens. Lastly, predictions of the strain-stress responses and Young's modulus of concrete calculated by means of the present model were compared with experimental data to verify the potential of the proposed theoretical framework.

## 2. Experiments

### 2.1. Material characterizations

The concrete specimen in the present study consists of a Portland Type I cement matrix (phase 0), normal aggregates (phase 1), CCB aggregates (phase 2), and microcrack (phase 3). It was assumed that the normal aggregates, CCB aggregates, and microcrack were uniformly distributed in the cement matrix. The elastic properties of the cement are as follows: $E_0$=30 GPa and $\nu_0$=0.20, where $E_0$ and $\nu_0$ denote the Young's modulus and Poisson's ratio of the cement matrix, respectively [11,12].

The normal aggregate applied in this study is metamorphic rock (quartzite) acquired from nature of the type commonly utilized at construction sites. The bulk density and absorption of water of the normal aggregate were measured and found to be 1490 kg/m$^3$ and 0.37%, respectively. In addition, the production process of the CCB aggregates is shown in Fig. 1. Initially, clay was taken from nature and sent to a mold to be formed into a brick shape. The bricks were produced through drying, heating, cooling processes and were finally crushed to be applied as a coarse aggregate for concrete. The bulk density and absorption of water of the CCB aggregates were 1130 kg/m$^3$ and 14.5%, respectively. It was found that the CCB aggregates are lighter than the normal aggregate and have a higher water absorption due to the inherent voids. The Portland Type I cement satisfying ASTM C150, which having specific gravity and Blaine surface area of 3.10 and 3400 cm$^2$/g, was used and the strength of the cement at 28 days measured following the ASTM C109 was 38 MPa. Crushed sand with the fineness modulus (FM) of 2.85, water absorption of 2.3% and specific gravity of 2.54 was used as fine aggregate. The grain size distribution of each type of aggregate is listed in the Appendix A.

The Young's modulus of normal and CCB aggregates should be measured for a theoretical study, but it was quite difficult to measure them accurately given the variation in their shapes. Hence, normal and CCB aggregates specimens were manually processed into specimens with a 1 cm$^3$ cubic shape and the stress-strain curves of the aggregate specimens for compressive loading were then estimated using a universal testing machine (UTM). The results of the compressive tests of the normal and CCB aggregates specimens are correspondingly presented in

**Table 1**
Compressive strength and Young's modulus of normal coarse aggregates.

| Sample | G1 | G2 | G3 | G4 | G5 | G6 | G7 | Avg. |
|---|---|---|---|---|---|---|---|---|
| Max. stress (MPa) | 91.6 | 309.4 | 62.0 | 194.3 | 38.0 | 76.7 | 285.3 | 151.0 ± 111.6 |
| Young's modulus (MPa) | 4622 | 34,221 | 2603 | 28,390 | 1901 | 1211 | 51,905 | 17836.1 ± 20320.4 |

**Table 2**
Compressive strength and Young's modulus of CCB aggregates.

| Sample | B1 | B2 | B3 | B4 | B5 | B6 | B7 | B8 | B9 | Avg. |
|---|---|---|---|---|---|---|---|---|---|---|
| Max. stress (MPa) | 17.1 | 18.6 | 17.9 | 21.4 | 5.9 | 17.9 | 10.3 | 26.6 | 7.2 | 15.9 ± 6.8 |
| Young's modulus (MPa) | 1119 | 557 | 1461 | 2304 | 570 | 1579 | 669 | 2650 | 350 | 1251.0 ± 816.3 |

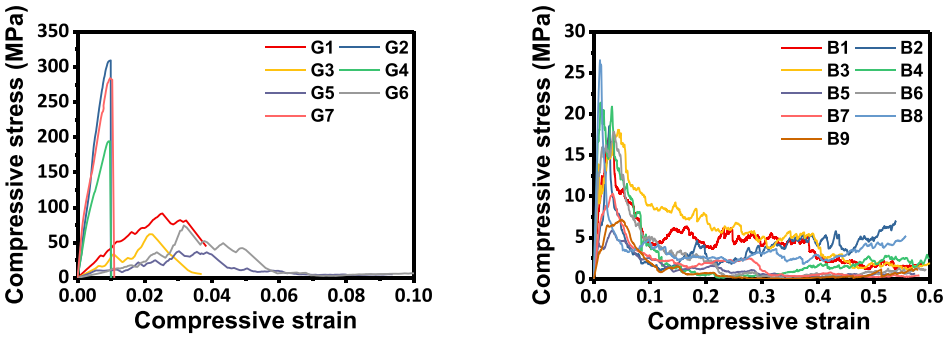


**Fig. 2.** Stress-strain curves of (a) normal and (b) CCB aggregate specimens.

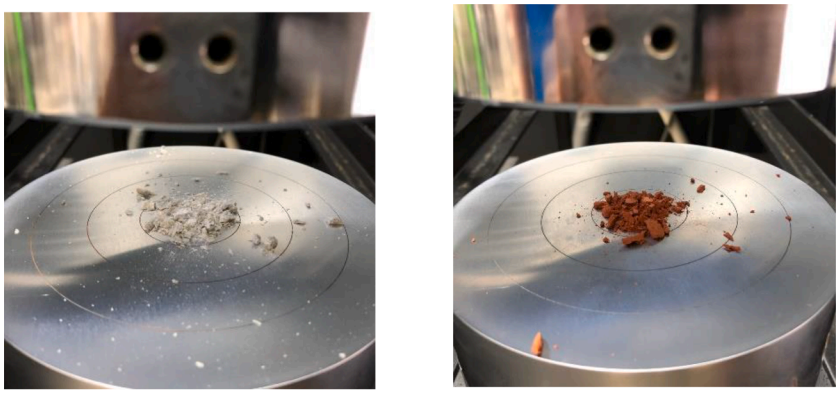


**Fig. 3.** Spreading patterns of broken (a) normal and (b) CCB aggregate specimens due to compressive loading.

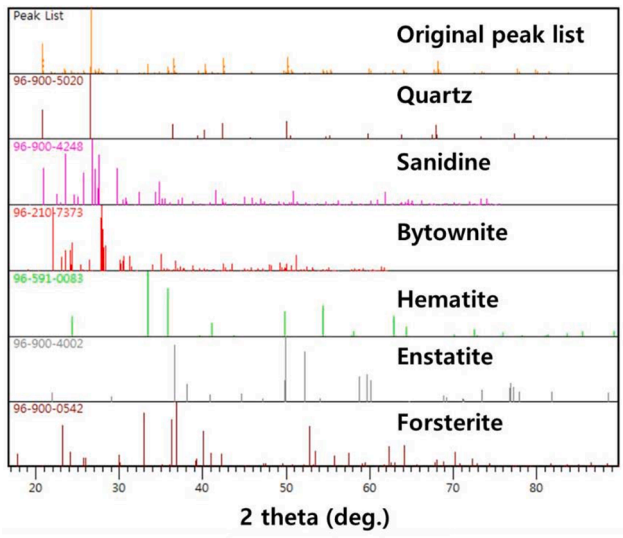


**Fig. 4.** XRD spectra of the CCB aggregate.

Tables 1 and 2 and in Figs. 2 and 3.

For the normal aggregate, it was clearly divided depending on whether or not high compressive strength was found. This is believed to be due to the randomness of the aggregates collected from nature. The average value of all measurement results was considered as a representative Young's modulus of the normal aggregate: $E_1$=151 GPa. For CCB aggregates, the mechanical properties were more even than those of the normal aggregate. This is believed to be due to the same process of artificial production of the CCB aggregates. The Young's modulus of the CCB aggregates was also assumed to be the average value of all test results as a representative value, in this case $E_2$=15.9 GPa. It is noted that more experiments were conducted on the CCB aggregates compared to the normal aggregate due to the lack of information in the literature on the CCB aggregates.

An X-ray diffraction (XRD) analysis was conducted to analyze the major components of the CCB aggregates. These results are shown in Fig. 4. The main component of the CCB aggregates was found to be quartz, and the normal aggregate was considered to be similar [13,14]. The Poisson's ratio of both the normal and the CCB aggregates are thus assumed to be $\nu_1$=$\nu_2$=0.16 [15].

**Table 3**
Mix proportions of the concrete.

| No. | Specimen | Mix proportion (kg/m3) | | | | |
|---|---|---|---|---|---|---|
| | | Water | Cement | Sand | Nor. agg. | CCB agg. |
| 1 | B0-0.45 | 193 | 430 | 722 | 1032 | 0 |
| 2 | B50-0.45 | | 430 | 722 | 516 | 395 |
| 3 | B100-0.45 | | 430 | 722 | 0 | 791 |
| 4 | B0-0.50 | | 387 | 764 | 1032 | 0 |
| 5 | B50-0.50 | | 387 | 764 | 516 | 395 |
| 6 | B100-0.50 | | 387 | 764 | 0 | 791 |
| 7 | B0-0.55 | | 352 | 800 | 1032 | 0 |
| 8 | B50-0.55 | | 352 | 800 | 516 | 395 |
| 9 | B100-0.55 | | 352 | 800 | 0 | 791 |
| 10 | B0-0.60 | | 322 | 828 | 1032 | 0 |
| 11 | B50-0.60 | | 322 | 828 | 516 | 395 |
| 12 | B100-0.60 | | 322 | 828 | 0 | 791 |
| 13 | B0-0.65 | | 297 | 854 | 1032 | 0 |
| 14 | B50-0.65 | | 297 | 854 | 516 | 395 |
| 15 | B100-0.65 | | 297 | 854 | 0 | 791 |
| 16 | B0-0.70 | | 276 | 874 | 1032 | 0 |
| 17 | B50-0.70 | | 276 | 874 | 516 | 395 |
| 18 | B100-0.70 | | 276 | 874 | 0 | 791 |

**Table 4**
Young's modulus of the concrete specimens.

| Specimen | w/c | S/a | CCB agg. Replacement Vol (%) | Young's modulus (GPa) | |
|---|---|---|---|---|---|
| | | | | Ave. | Stan. dev. |
| B0-0.45 | 0.45 | 0.411 | 0 | 25.09 | 5.19 |
| B50-0.45 | | | 50 | 20.76 | 7.57 |
| B100-0.45 | | | 100 | 9.94 | 0.56 |
| B0-0.50 | 0.50 | 0.425 | 0 | 24.60 | 5.51 |
| B50-0.50 | | | 50 | 12.75 | 4.07 |
| B100-0.50 | | | 100 | 7.45 | 3.19 |
| B0-0.55 | 0.55 | 0.436 | 0 | 18.22 | 5.35 |
| B50-0.55 | | | 50 | 21.58 | 6.68 |
| B100-0.55 | | | 100 | 12.27 | 4.35 |
| B0-0.60 | 0.60 | 0.445 | 0 | 23.65 | 0.26 |
| B50-0.60 | | | 50 | 16.99 | 3.15 |
| B100-0.60 | | | 100 | 6.78 | 2.70 |
| B0-0.65 | 0.65 | 0.453 | 0 | 15.53 | 1.06 |
| B50-0.65 | | | 50 | 15.98 | 1.57 |
| B100-0.65 | | | 100 | 10.28 | 1.60 |
| B0-0.70 | 0.70 | 0.459 | 0 | 17.65 | 3.48 |
| B50-0.70 | | | 50 | 9.79 | 2.56 |
| B100-0.70 | | | 100 | 12.50 | 1.96 |

### 2.2. Concrete specimens and results

Concrete specimens were prepared with various CCB aggregates replacement rates and w/c ratios. Here, 0, 50, and 100% were the CCB substitution rates, and the w/c ratios used were 0.45, 0.50, 0.55, 0.60, 0.65, and 0.70. Hence, eighteen different mix proportions were designed to investigate the effects of the concrete constituents, as summarized in Table 3. In the mix proportions, the target compressive strength was not considered, but the slump and maximum size of the coarse aggregate, including normal and CCB aggregates, were adjusted as 80 mm and 25 mm, respectively. The labels of the specimens were determined according to the variables. For instance, B0-0.45 denotes a concrete specimen with a w/c ratio of 0.45 without any CCB aggregates. On the other hand, B50-0.60 refers to a concrete specimen with a w/c ratio of 0.60 in which 50% of the normal aggregate is substituted with CCB aggregates.

The unit weight of water was fixed for all mixtures, regardless of w/b or CCB aggregate content. In the conventional mix proportion method for structural concrete with limited amount of water reducer such as ACI 211.1, the water content in the concrete may vary by diverse factors such as maximum size of coarse aggregates, target consistency, and air content. However, in recent years, the consistency and air content of fresh concrete can be controlled by the chemical agent including high-range water reducer or air entraining agent, rather than adjusting the water content.

The fabrication of the present concrete specimens proceeded as follows: a desired amount of a binder and aggregate (sand, normal, and CCB) was placed in a mixer and stirred for 2 min to ensure homogeneity of the mixture [16]. Thereafter, water was poured into the mixer and was stirred for additional 2 min [17]. The fresh concrete was then introduced into a cylindrical mold with dimensions of $\phi 100 \times 200$ mm. All specimens were cured in an unsealed condition until the designated compressive strength test day.

To evaluate the mechanical behavior of the concrete specimens, a series of compressive strength tests were conducted in accordance with ASTM C39. The compressive strength tests were carried out using a 250 kN load cell connected to an INSTRON 5985 machine (INSTRON Inc.) to determine the applied stress and strain values. Detailed test procedures can be found in ASTM C39, and the test results of the Young's moduli and compressive strength are listed in Table 4. Overall, the mechanical properties of the Young's modulus and compressive strength decreased as the CCB aggregates replacement ratio and w/c ratio were increased. Representative fracture surfaces of concrete with normal and CCB aggregates are presented in Fig. 5.

## 3. Modeling of concrete with normal and CCB aggregates

### 3.1. Micromechanics-based constitutive equation

In the most studies on the mechanical properties of concrete with porous aggregates, the classical continuum mechanics model counted in the porosity-strength relationship was generally applied [18,19].

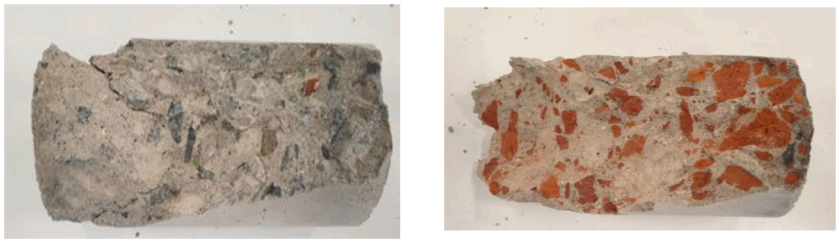

(a) (b)

**Fig. 5.** Representative fracture surfaces of concrete with (a) normal and (b) CCB aggregates.

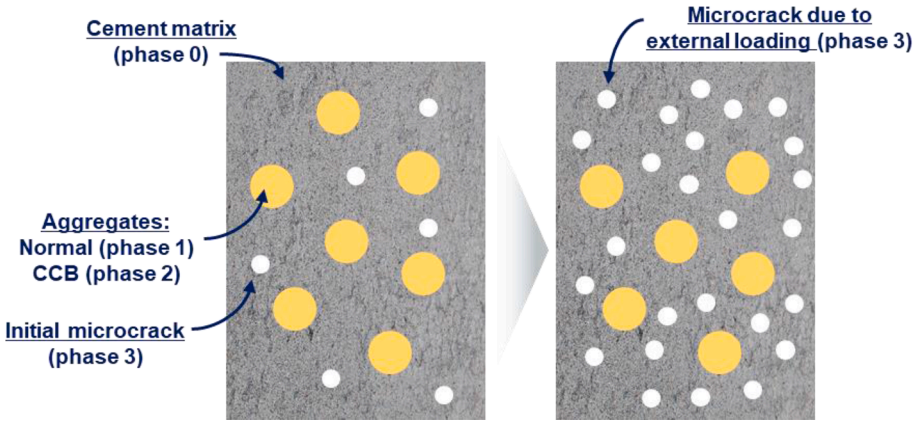


**Fig. 6.** Schematic diagram of concrete mixed with normal and CCB aggregates: (left) initial state; (right) equivalent damaged state (microcracks).

However, in this case, it was hard to draw a unified constituent model for these types of concrete because of the large fluctuation of the data depending on the type of aggregate. On the other hand, some of ML-based models for the mechanical properties of concrete has been proposed and, in the most of them, the mechanical properties of concrete were directly linked with the physical characteristics of aggregates [20,21]. This approach was straightforward and easy to apply, but this numerical linking was theoretically unclear. In this study, the ML-based approach was utilized to obtain the numerical relationship between the properties of porous aggregate and the parameters used in the continuum mechanics-based micromechanical model, which had been found with try-and-error method in previous works. This modeling technique has the potential to construct a general constituent model when data on various types of aggregates are sufficiently accumulated.

The representative volume element (RVE) of concrete was composed of an isotopically cement matrix (phase 0), uniformly and randomly distributed aggregates (phases 1 and 2), and a microcrack (phase 3) [22]. The aggregates were defined as having different phases (1 and 2) so that they could be separately applied as normal and CCB aggregates according to the mix proportion. In addition, it was assumed that microcracks existed inside the concrete at the beginning and that they gradually increased due to external loading to reduce the mechanical characterization of specimen. A schematic illustration of the initial state and the equivalent damaged state of concrete mixed with normal and CCB aggregates is presented in Fig. 6. Concrete generally contains about 0.5–5% of voids inevitably [23], and the amount thereof increases as external stress is applied [24]. The external stress causes a stress concentration around interfaces between cement and aggregate/void, and these phenomena accelerate material failure [25,26]. In this study, considering these material properties and mechanical theories, the initial voids were assumed to be microcracks. In addition, assuming that these microcracks gradually increase as external stress is applied, the proposed constitutive equation was derived. Images for Portland type I cement matrix (phase 0), normal aggregates (phase 1), CCB aggregates (phase 2), and microcracks (phase 3) are illustrated in the Appendix B.

The effective stiffness tensor C* of concrete could then be derived, as follows [27–29]:

$$\mathrm{C}^{*} = \mathrm{C}_0 \cdot \left[\mathrm{I} + \mathrm{B} \cdot (\mathrm{I} - \mathrm{S} \cdot \mathrm{B})^{-1}\right] \tag{1}$$

with

$$\mathrm{A}_r = (\mathrm{C}_r + \mathrm{C}_0) \cdot \mathrm{C}_0 \tag{2}$$

and

$$\mathrm{B} = \sum_{r=1}^{3} \left\{ \phi_r (\mathrm{S} + \mathrm{A}_r)^{-1} \right\} \tag{3}$$

where $\mathrm{C}_r$ and $\phi_r$ correspondingly signify the elasticity tensor and volume fraction of the $r$-phase, I is the fourth-rank identity tensor, and S denotes the Eshelby's tensor for a spherical inclusion, defined as [30,31] follows:

$$\mathrm{S} = \frac{1}{15(1-\nu_0)}\left[(5\nu_0 - 1)\delta_{ij}\delta_{kl} + (4 - 5\nu_0)\left(\delta_{ik}\delta_{jl} + \delta_{il}\delta_{jk}\right)\right] \tag{4}$$

In this equation, $\nu_0$ indicates the Poisson's ratio of the cement matrix and $\delta_{ij}$ denotes the Kronecker delta. By carrying out a lengthy algebraic process, the component of the fourth-rank tensor C* can be explicitly derived as

$$\mathrm{C}^{*} = \lambda^{*}\delta_{ij}\delta_{kl} + \mu^{*}\left(\delta_{ik}\delta_{jl} + \delta_{il}\delta_{jk}\right) \tag{5}$$

where $\lambda^*$ and $\mu^*$ correspondingly denote the Lame constant and shear modulus, which can be written as follows:

$$\lambda^{*} = \kappa_0\left[1 + \sum_{r=1}^{3}\frac{30(1-\nu_0)\phi_r}{3\alpha_r + 2\beta_r - 10(1+\nu_0)\phi_r}\right] - \frac{2}{3}\left[1 + \sum_{r=1}^{3}\frac{15(1-\nu_0)\phi_r}{\beta_r - 2(4-5\nu_0)\phi_r}\right]$$

$$\mu^{*} = \mu_0\left[1 + \sum_{r=1}^{3}\frac{15(1-\nu_0)\phi_r}{\beta_r - 2(4-5\nu_0)\phi_r}\right] \tag{6}$$

where $\kappa_r$ and $\mu_r$ are the bulk and shear modulus of the $r$-phase, respectively. These can be defined as $\kappa_r = E_r/[3(1-2\nu_r)]$ and $\mu_r = E/(1+\nu_r)$. The parameters of $\alpha_r$ and $\beta_r$ can be expressed as

$$\alpha_r = \frac{1}{3}\left[\frac{\kappa_0}{\kappa_r - \kappa_0} - \frac{\mu_0}{\mu_r - \mu_0}\right], \beta_r = \frac{1}{2}\frac{\mu_0}{\mu_r - \mu_0}(r = 1\text{and}2)$$

$$\alpha_3 = 2(5\nu_0 - 1), \beta_3 = -15(1-\nu_0) + 2(4-5\nu_0) \tag{7}$$

The volume fractions of the normal and CCB aggregates ($\phi_1$ and $\phi_2$) are manually input according to the mix proportions, and the volume fraction of the microcracks ($\phi_3$) in the concrete is calculated through the following isotropic scalar function [32–34]:

$$\phi_3 = \begin{cases} \phi_{3,initial}, \varepsilon^{th} < \varepsilon^{a} \\ \phi_{3,initial} + c_1\left(1 - \dfrac{\varepsilon^{th}}{\varepsilon^{a}}\right)^{c_2}, \varepsilon^{th} > \varepsilon^{a} \end{cases}$$

Here, $\varepsilon^a$ represents the effective macroscopic strain [34]. $\varepsilon^{th}$, $\phi_{3,\text{initial}}$, $c_1$, and $c_2$ are the model parameters in this study and are defined as follows: $\varepsilon^{th}$=threshold effective strain of a microcrack, $\phi_{3,\text{initial}}$=initial volume fraction of the microcracks, $c_1$=nucleation parameter of the microcrack shape, and $c_2$=nucleation parameter of the microcrack distribution. The volume fraction of the cement matrix can be then calculated using the equation $\phi_0 = 1-(\phi_1+\phi_2+\phi_3)$ [29].

The proposed micromechanical model is based on the ensemble volume averaged approach [30,35], and the local solution of the

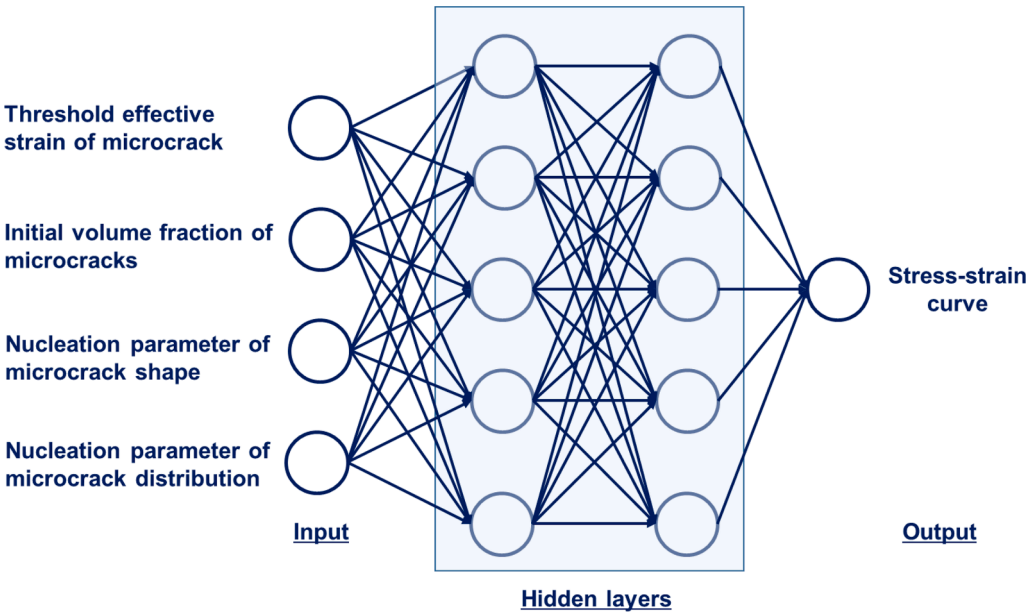


**Fig. 7.** Schematic diagram of the GA algorithm adopted in the present study.

inclusion interaction problem is not theoretically considered. The noninteracting approximation is advantageous for mathematical simplicity; however, the proposed approach may be limited when the inclusion content increases. In addition, the long-term performance of concrete was not investigated in this study. This study was carried out by focusing on the analysis of the elastic region, which is beyond the scope of the present study. However, we plan to extend our work along this direction in the near future [31].

### 3.2. ML and FE techniques

For more accurate predictions, it is necessary to consider the nonlinear damage of the material. However, it is nearly impossible quantitatively to determine the exact nucleation point and progressive pattern of certain types of nonlinear damage, such as a microcrack. Therefore, in most cases, the damage parameters are set as model constants and corresponding values are fitted through a comparison with experimental outcomes. It is, however, very difficult and time-consuming manually to determine numerous model constants that satisfy various experimental results. A combination of several model constants may accidentally agree well with the experimental results, and duplicate prediction results may be derived depending on the specific combination of parameters used [36].

Hence, we attempted to estimate the optimal model constant values of the present micromechanics-based constitutive equation through a ML technique, in this case a GA. The GA approach is known to be guaranteed to converge to an optimal solution of multivariable functions by repeating generations of a population, fitness and/or penalty evaluations, preferences, re-production, crossover, and mutations [37,38]. GA-based optimization has the advantage of finding solutions for more diverse variables through a chromosome approach.

The model constants that require handling in this study are $P_{set}=[\varepsilon^{th}, \phi_{3,initial}, c_1, c_2]$, which are related to microcracks in the derived constitutive equation. In addition, the corresponding output value was set as stress-strain curves composed of relatively large amounts of data. A schematic diagram of GA algorithm adopted in the present study is presented in Fig. 7. The range and interval of each of the constants were set as follows: $\varepsilon^{th}=[0, 0.003]$ at an interval of 0.0001, $\phi_{3,initial}=[0, 0.15]$

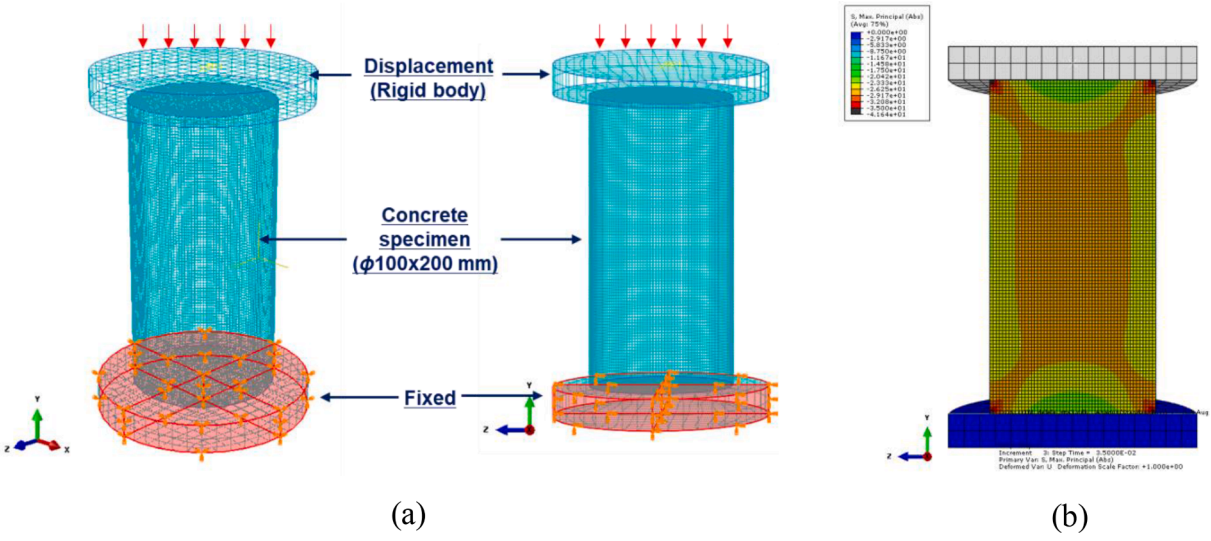


**Fig. 8.** (a) FE model with boundary conditions and (b) the representative maximum principal stress distribution of the concrete specimen.

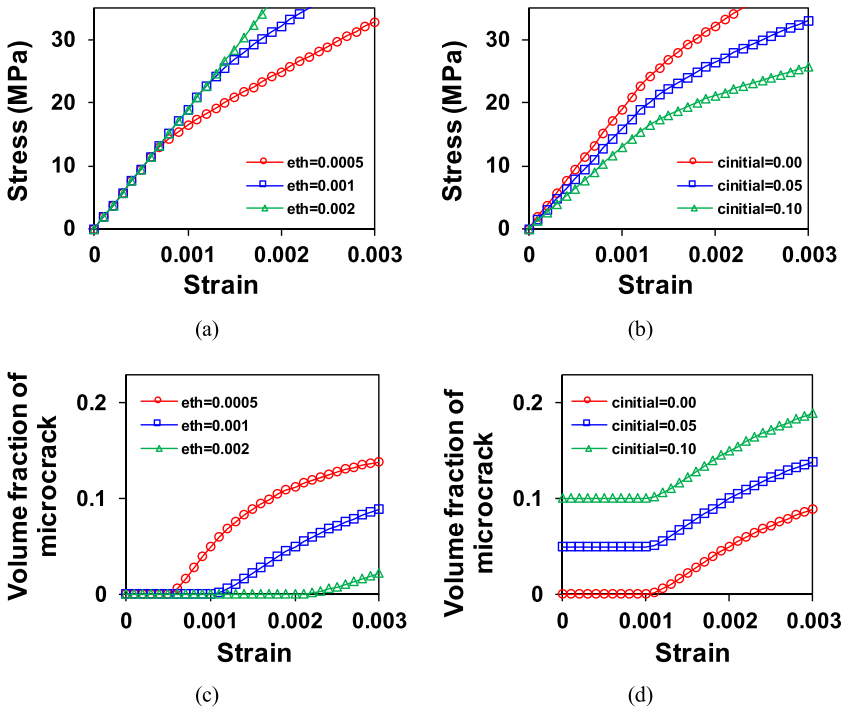


**Fig. 9.** Parametric study results: the predicted stress-strain responses of concrete when varying the (a) threshold effective strain ($\varepsilon^{th}$) and (b) initial density of the microcracks ($\phi_{3,\ initial}$); microcrack evolution versus the strain when varying the (a) $\varepsilon^{th}$ and (b) $\phi_{3,\ initial}$ values.

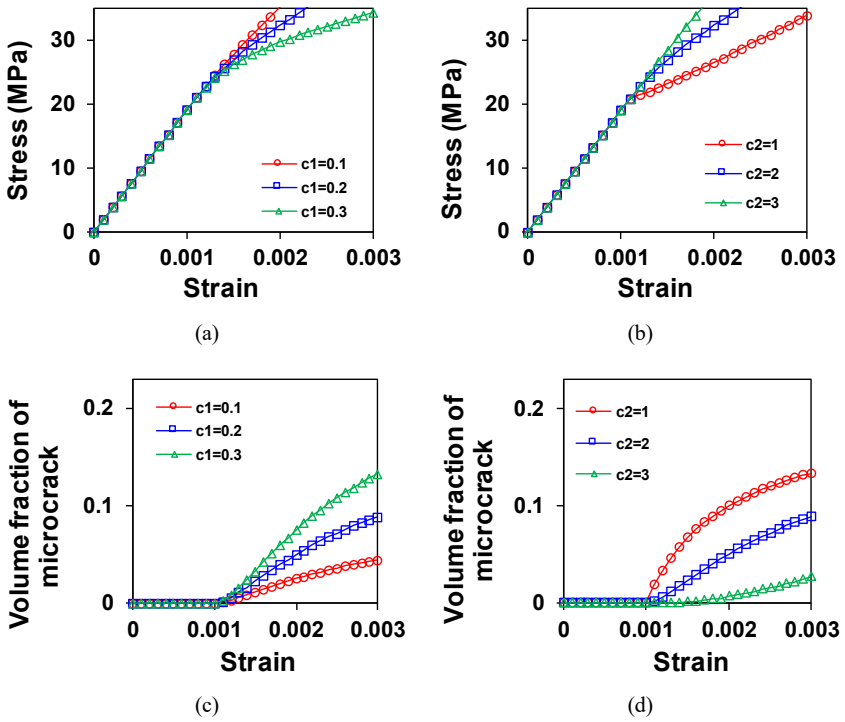


**Fig. 10.** Parametric study results: the predicted stress-strain responses of concrete when varying the nucleation parameter of the (a) microcrack shape ($c_1$) and (b) microcrack distribution ($c_2$); microcrack evolution versus the strain when varying the (a) $c_1$ and (b) $c_2$ values.

at an interval of 0.01, and $c_1$ and $c_2$=[0, 5] at an interval of 0.1. A more detailed description of the contents of the procedure and the theoretical background of the GA can be found in the literature [38,39].

The constitutive equation with the optimal microcrack model contestant was then implemented into the FE code ABAQUS through a user subroutine technique (UMAT). An FE model was constructed to describe the outcome similarly to the actual experiment, the details of which are shown in Fig. 8. A cylindrical FE model identical in size to the

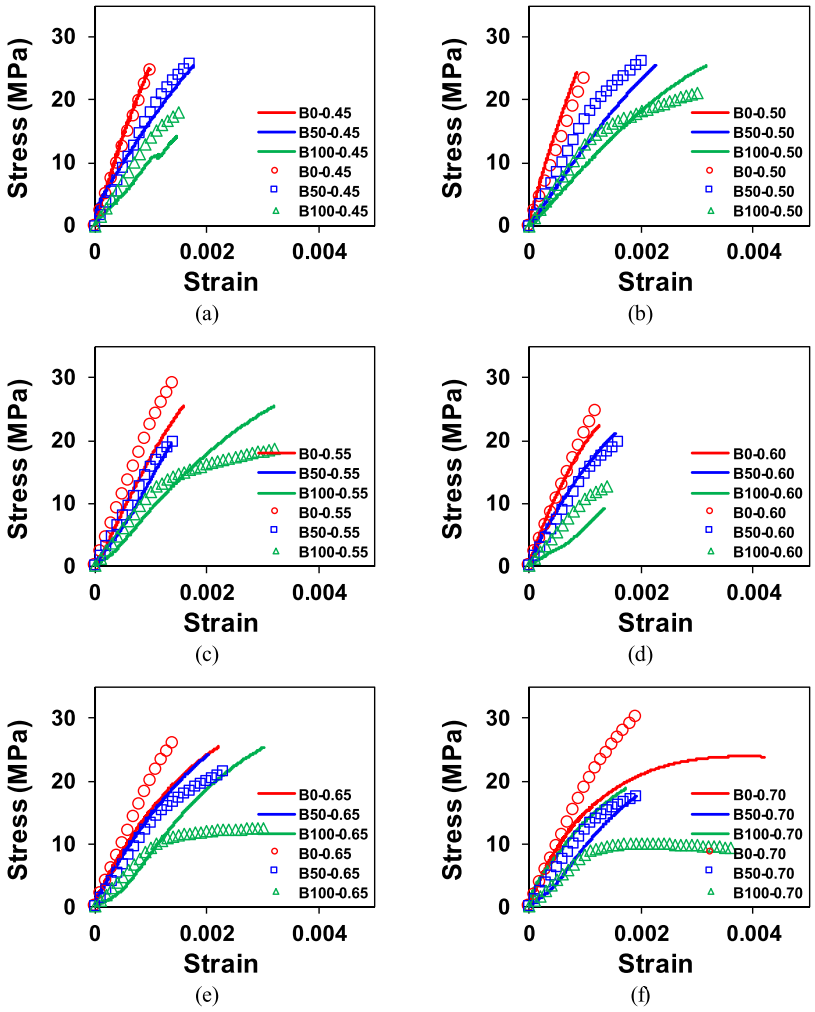


**Fig. 11.** Experimental comparisons of the stress-strain curves (line: measurements, symbol: predictions).

specimen utilized in the experiment is located between the upper load cell and the lower jig [40]. The jig model was fixed in all directions, and the load cell model set as a rigid body was designed to move from top to bottom. Fig. 8(a) and (b) show the FE model with boundary conditions and the representative stress distribution of the concrete specimen, respectively.

## 4. Numerical analysis experimental comparisons

A series of numerical analyses were carried out to investigate the influences of the model constants ($\varepsilon^{th}$, $\phi_{3,\text{initial}}$, $c_1$, and $c_2$) on the mechanical behaviors of the concrete specimens. Concrete in which half normal and half CCB aggregates are mixed was considered; the material constant values applied in this numerical analysis are as follows: $E_0$=3.00 GPa, $\nu_0$=0.20; $E_1$=17.84 GPa, $\nu_1$=0.16; $E_2$=1.25 GPa, and $\nu_2$=0.16; $E_3$=$\nu_3$=0. The model constants of microcracks applied in the numerical analysis were $\varepsilon^{th}$=[0.0005–0.002], $\phi_{3,\text{initial}}$=[0.0–1.0], $c_1$=[0.1–0.3], and $c_2$=[1–3]. Figs. 9 and 10 show the test results of the numerical analysis.

First, the effects of $\varepsilon^{th}$ and $\phi_{3,\text{initial}}$ were determined, as shown in Fig. 9. The stress-strain response of the concrete becomes stiffer as $\varepsilon^{th}$ increases (Fig. 9(a)), while a lower stiffness of concrete was predicted as the $\phi_{3,\text{initial}}$ value increases (Fig. 9(b)). This indicates that the nucleation of a microcrack gradually occurs later as $\varepsilon^{th}$ increases, resulting higher effective stiffness of the concrete. However, a higher value of $\phi_{3,\text{initial}}$ indicates that the concrete contains numerous micro-voids, which in turn reduces the stiffness of the material. The predicted microcrack evolution of the concrete corresponding Fig. 9(a) and (b) are given in Fig. 9(c) and (d). Fig. 9(c) and (d) depict the microcrack evolution according to the occurrence of strain ($\varepsilon^{th}$) and the volume fraction of the initial microcrack ($\phi_{3,\text{initial}}$). It can be seen in Fig. 9 that the model constants have a considerable influence on the evolution of the microcrack and the effective stiffness of the concrete.

The effects of model constants $c_1$ and $c_2$ are presented in Fig. 10. The same material properties applied in the previous numerical tests were adopted in the simulation here. Fig. 10(a) and (b) show the predicted effective stiffness of concrete with varying values of $c_1$ and $c_2$. It can be seen in Fig. 10(a) that the effective stiffness of the concrete decreases gradually when value of $c_1$ increases. It is also predicted that a lower value of $c_2$ will lead to the rapid nucleation of a microcrack, reducing the stiffness of the concrete [40]. In addition, the predicted evolution of the volume fraction of microcracks corresponding to Fig. 10(a) and (b) are shown in Fig. 10(c) and (d), respectively.

Although there were some fluctuations on the experimental results, a tendency can be observed in Fig. 11 that the Young's moduli of concrete were lower with larger w/c and higher contents of CCB aggregate in the concrete. It was the result of affecting the increase of the voids in the concrete according to the increase of w/c. In addition, it was believed that the decrease in Young's moduli according to the increase in CCB aggregate content is due to the relatively low modulus of elasticity of the CCB. The Young's modulus of normal aggregate was 17.84 GPa, whereas

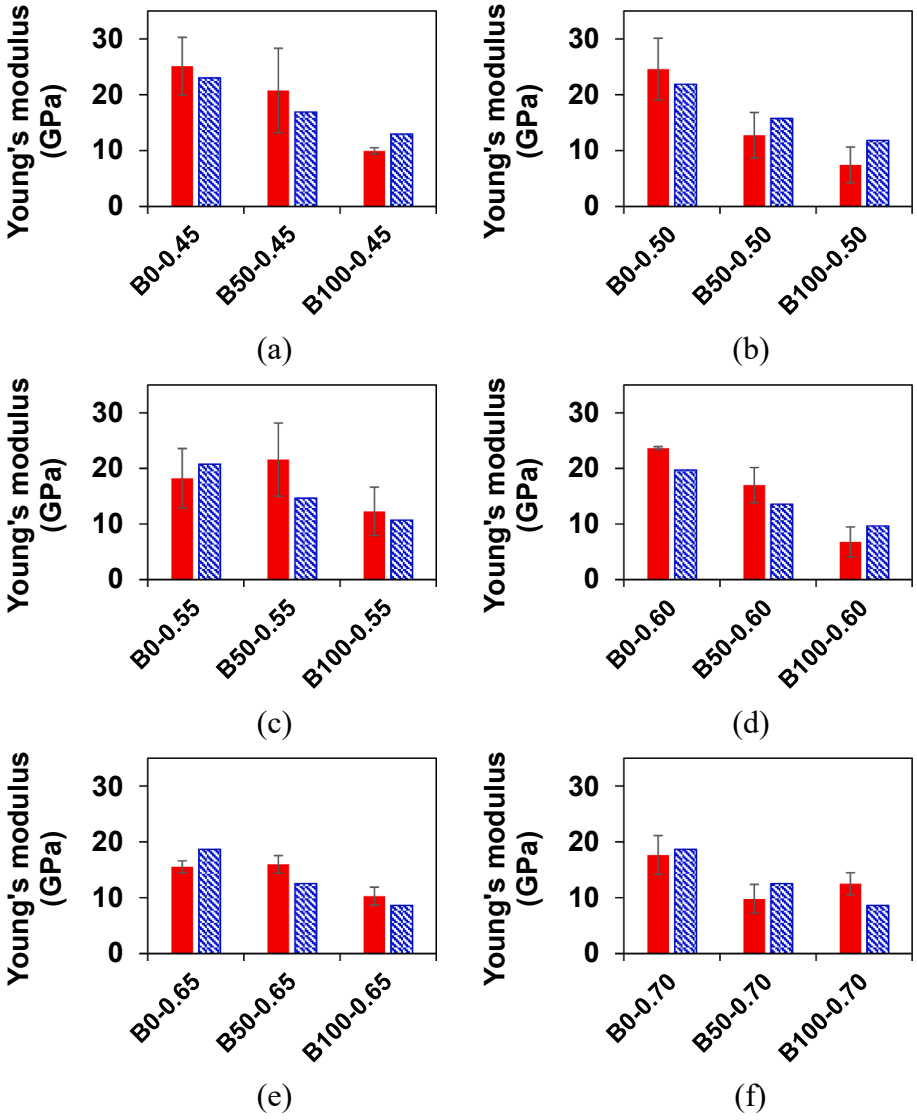


**Fig. 12.** Experimental comparisons of the Young's modulus (red solid: measurements, blue line: predictions).

that of CCB aggregate was 1.25 GPa, which was about 14.2 times higher than that of normal aggregate. This physical difference between the two aggregates is thought to have affected the compressive strength of the specimens. The compressive strength of the specimens was indicated in the Appendix C. Similar to the Young's modulus, the compressive strength tends to decrease with increasing w/c and content of CCB aggregate. It is noted that the theoretical framework applied in the present study is an analysis within an elastic region, and thus has a limitation in accurately predicting compressive strength.

To elucidate the proposed theoretical framework, various comparisons between the experimental results and predictions are made, as illustrated in Figs. 11 and 12. The results of the comparison of the stress-strain curves of concrete with respect to the replacement rate of the CCB aggregates and w/c ratio are shown in Fig. 11. The adopted materials constants are identical to the values used for the numerical analysis. The estimated microcrack constants based on the GA are $\varepsilon^{th}$=0.0008, $\phi_{3,initial}$=0.06, $c_1$=0.2, and $c_2$=2. Herein, we judge that it would be more realistic for the volume ratio of the initial microcracks to differ according to the w/c ratio; thus, the following simple equation is applied: $\phi_{3,initial}$=0.4(w/c−0.45)+0.01. Overall, Fig. 11 shows a good correlation between the test results and the predictions in the range of w/c=0.45–0.60. However, it was observed that the prediction accuracy decreased as the w/c ratio was increased (w/c ratio≥0.65).

It has been known that, in the case of an artificial lightweight aggregate with a very uniform internal microstructure, the elastic modulus of the aggregate and that of the surrounding cement mortar are similar, and the strain-stress curve were linear up to the fracture stress [41]. On the other hand, in the case of CCB aggregates that are produced by crushing and may already have irregular microcracks inside [42], the nonlinearity of the strain-stress curve might be higher as the cracks in the aggregate might be propagated during the loading of concrete. As shown in Fig. 11, the nonlinearity of the strain-stress curve became larger in the concrete containing higher content of CCB aggregate, which made it very difficult to obtain the structural Young's modulus of the concrete. It should be noted that the use of this ML-based approach could be an effective solution in this nonlinear behavior.

This occurred because the w/c ratio has a major effect on the overall behavior of the concrete. The w/c ratio of concrete affects numerous factors, such as the cement-aggregates interphase, the chemical hydrate reaction, and the segregation resistance, among others [1,2]. Nonlinear microcrack damage is not sufficient to account for all of the effects of the w/c ratio on concrete, which is a limitation of the present theoretical model. In general, it is rare for concrete to have a w/c ratio exceeding 0.65. Accordingly, the proposed model can be said to be an approach

**Table 5**
Particle size distribution of CCB and normal aggregates [42]

| Sieve size (mm) | Cumulative passing (%) | | Sieve size (mm) | Cumulative passing (%) | Sieve size (mm) | Cumulative passing (%) |
|---|---|---|---|---|---|---|
| | ASTM C330 Requirement (max.) | ASTM C330 requirement (min.) | | Normal agg. | | CCB agg. |
| 37.5 | 100 | 95.0 | 37.5 | 100.0 | 37.5 | 100.0 |
| 12.5 | 60 | 25.0 | 19.0 | 76.4 | 19.0 | 67.0 |
| 4.75 | 25 | 0.0 | 9.50 | 10.4 | 9.50 | 17.4 |
| 0.075 | 10 | 0.0 | 4.75 | 0.9 | 4.75 | 5.7 |
| | | | 0.0 | 0.0 | 3.35 | 3.2 |
| | | | | | 2.36 | 2.9 |
| | | | | | 1.18 | 2.7 |
| | | | | | 0.0 | 0.0 |

that reasonably simulates most cases. However, further studies of the effect of surplus water due to such an excessive w/c ratio are required.

Furthermore, the predicted Young's modulus values of concrete with respect to the aggregate replacement rate and the w/c ratio are compared with the experimental results obtained in the present study. Note that the same material and microcrack parameters previously used were applied as well in this comparison to verify the theoretical effectiveness of the model. Regarding the Young's modulus, it was observed that the predicted values were in fairly good agreement with the experimental results in most cases. In the experiment, the tendency of the Young's modulus according to the material constituents varies depending on numerous mechanisms. However, in the theoretical analysis, the Young's modulus was predicted to decrease constantly as the CCB substitution rates and w/c ratios were increased.

## 5. Conclusions

The present study proposed a theoretical strategy that relies on experiments, micromechanics, and a ML technique to predict the mechanical behaviors of concrete mixed with different types of aggregates. The following key conclusions are summarized:

1. Concrete specimens were prepared with varying normal/CCB aggregates replacement rates and w/c ratios. As a result of the experiment, low effective stiffness and Young's modulus outcomes were found when the CCB aggregates replacement rate and the w/c ratio were high.
2. A micromechanical constitutive equation for the concrete containing multi-phase aggregates was derived and implemented into a FE analysis. The optimal value of nonlinear parameter, microcrack constants, was estimated by combining experimental data and ML algorithm. The optimized model constants are $\varepsilon^{th}$=0.0008, $\phi_{3,\text{initial}}$=0.06, $c_1$=0.2, and $c_2$=2.
3. The stress-strain responses and Young's modulus of the concrete specimen were predicted based on the proposed model, and in most cases, they were in good agreement. However, the prediction accuracy with a high w/c ratio (w/c $\geq$ 0.65) was low.

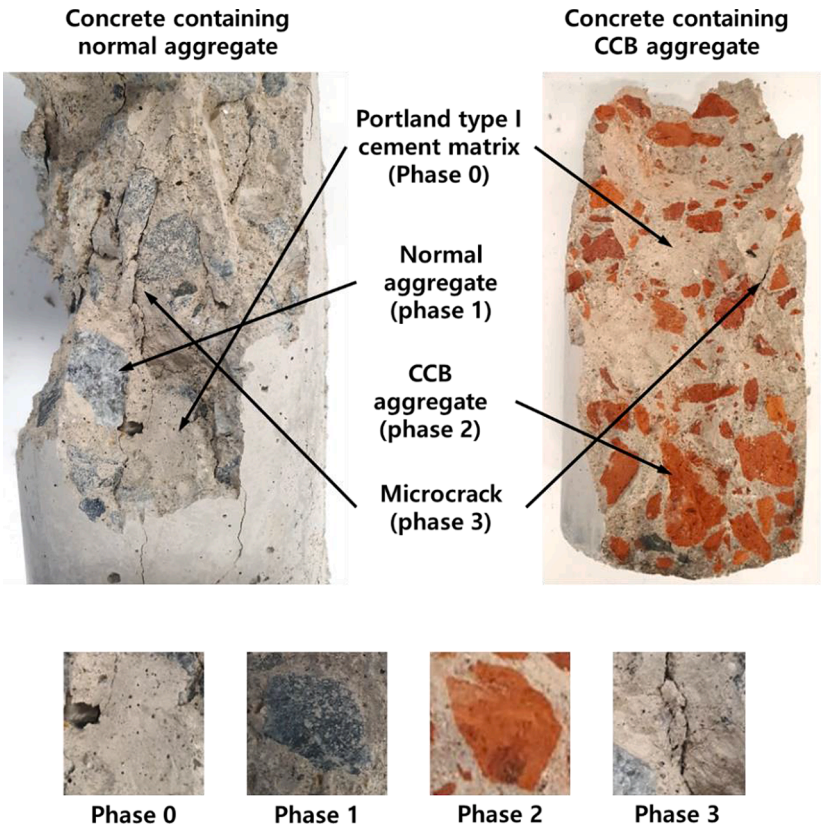


**Fig. 13.** Images for Portland type I cement matrix (phase 0), normal aggregate (phase 1), CCB aggregate (phase 2), and microcrack (phase 3).

**Table 6**
Compressive strength of concrete specimens [42]

| Specimen | w/c | S/a | Brick chip replacement (vol.%) | Compressive strength (MPa) | |
|---|---|---|---|---|---|
| | | | | 7 d | 28 d |
| B0-0.45 | 0.45 | 0.411 | 0 | 29.2 | 33.0 |
| B50-0.45 | | | 50 | 31.8 | 32.7 |
| B100-0.45 | | | 100 | 24.0 | 22.4 |
| B0-0.50 | 0.50 | 0.425 | 0 | 32.8 | 37.4 |
| B50-0.50 | | | 50 | 28.9 | 33.8 |
| B100-0.50 | | | 100 | 24.2 | 26.4 |
| B0-0.55 | 0.55 | 0.436 | 0 | 29.6 | 33.1 |
| B50-0.55 | | | 50 | 26.3 | 29.3 |
| B100-0.55 | | | 100 | 24.2 | 28.5 |
| B0-0.60 | 0.60 | 0.445 | 0 | 26.2 | 30.4 |
| B50-0.60 | | | 50 | 23.8 | 27.2 |
| B100-0.60 | | | 100 | 21.9 | 26.4 |
| B0-0.65 | 0.65 | 0.453 | 0 | 23.7 | 27.3 |
| B50-0.65 | | | 50 | 21.0 | 22.0 |
| B100-0.65 | | | 100 | 15.8 | 26.1 |
| B0-0.70 | 0.70 | 0.459 | 0 | 19.8 | 24.5 |
| B50-0.70 | | | 50 | 19.8 | 24.9 |
| B100-0.70 | | | 100 | 18.4 | 25.3 |

Based on the present model, a good correlation was found between the test results and predictions in the range of w/c=0.45–0.60. However, it was observed that the prediction accuracy decreased as the w/c ratio was increased (w/c ratio≥0.65). This occurred because the w/c ratio has fairly considerable effects on the overall mechanical/chemical properties of the concrete. Considering all of the effects of the w/c ratio on concrete exceeds the scope of the present study. Therefore, further studies should be carried out to investigate theoretically the effects of surplus water stemming from an excessive w/c ratio.

*CRediT authorship contribution statement*

**Hyeong-Ki Kim:** Writing – original draft, Conceptualization, Methodology. **Yeonggyu Lim:** Data curation, Investigation. **Million Tafesse:** . **G.M. Kim:** Conceptualization, Validation. **Beomjoo Yang:** Writing – review & editing, Supervision.

## Declaration of Competing Interest

The authors declare that they have no known competing financial interests or personal relationships that could have appeared to influence the work reported in this paper.

## Acknowledgements

This study was supported by a grant (21CTAP-C163988-01) from Ministry of Land, Infrastructure and Transport (MOLIT) of Korea government and Korea Agency for Infrastructure Technology Advancement (KAIA). In addition, this research was supported by the Basic Research Project of the Korea Institute of Geoscience and Mineral resources (KIGAM) funded by the Ministry of Science, ICT and Future Planning of Korea (GP2020-021).

## Appendix A. Appendix A. Particle size distribution of CCB and normal aggregates [42]

Table 5

## Appendix B. Images for Portland type I cement matrix (phase 0), normal aggregate (phase 1), CCB aggregate (phase 2), and microcrack (phase 3)

Fig. 13

## Appendix C. Compressive strength of concrete specimens [42]

Table 6

## References

[1] P.K. Mehta, P.J. Monteiro, Concrete: Microstructure, Properties, and Materials, McGraw-Hill Education, 2014.
[2] S. Mindess, J.F. Young, Concrete, Prentice Hall, 2002.
[3] A. Padmini, K. Ramamurthy, M. Mathews, Influence of parent concrete on the properties of recycled aggregate concrete, Construction and Building Materials 23 (2) (2009) 829–836.
[4] V.W. Tam, M. Soomro, A.C.J. Evangelista, A review of recycled aggregate in concrete applications (2000–2017), Construction and Building Materials 172 (2018) 272–292.
[5] S. Roh, R. Kim, W.-J. Park, H. Ban, Environmental Evaluation of Concrete Containing Recycled and By-Product Aggregates Based on Life Cycle Assessment, Applied Sciences 10 (21) (2020) 7503.
[6] E. Del Rey Castillo, N. Almesfer, O. Saggi, J.M. Ingham, Light-weight concrete with artificial aggregate manufactured from plastic waste, Construction and Building Materials 265 (2020), 120199.
[7] R. Islam, T.H. Nazifa, A. Yuniarto, A.S. Uddin, S. Salmiati, S. Shahid, An empirical study of construction and demolition waste generation and implication of recycling, Waste Management 95 (2019) 10–21.
[8] C. Zheng, C. Lou, G. Du, X. Li, Z. Liu, L. Li, Mechanical properties of recycled concrete with demolished waste concrete aggregate and clay brick aggregate, Results in Physics 9 (2018) 1317–1322.
[9] Y. Zhao, J. Gao, F. Chen, C. Liu, X. Chen, Utilization of waste clay bricks as coarse and fine aggregates for the preparation of lightweight aggregate concrete, Journal of Cleaner Production 201 (2018) 706–715.
[10] P. Pongsopha, P. Sukontasukkul, T. Phoo-ngernkham, T. Imjai, P. Jamsawang, P. Chindaprasirt, Use of burnt clay aggregate as phase change material carrier to improve thermal properties of concrete panel, Case Studies in Construction Materials 11 (2019), e00242.
[11] P. Trtik, J. Kaufmann, U. Volz, On the use of peak-force tapping atomic force microscopy for quantification of the local elastic modulus in hardened cement paste, Cement and concrete research 42 (1) (2012) 215–221.
[12] C. Hu, Z. Li, Micromechanical investigation of Portland cement paste, Construction and Building Materials 71 (2014) 44–52.
[13] N. Marinoni, M.A. Broekmans, Microstructure of selected aggregate quartz by XRD, and a critical review of the crystallinity index, Cement and Concrete Research 54 (2013) 215–225.
[14] D. Vollprecht, M. Berger, I. Altenburger-Junker, S. Neuhold, K.P. Sedlazeck, A. Aldrian, J.J. Dijkstra, A. van Zomeren, J.G. Raith, Mineralogy and leachability of natural rocks–A comparison to electric arc furnace slags, Minerals 9 (8) (2019) 501.
[15] H. Gercek, Poisson's ratio values for rocks, International Journal of Rock Mechanics and Mining Sciences 44 (1) (2007) 1–13.
[16] H.M. Park, S. Park, I.-J. Shon, G. Kim, S. Hwang, M.W. Lee, B. Yang, Influence of Portland cement and alkali-activated slag binder on the thermoelectric properties of the p-type composites with MWCNT, Construction and Building Materials 292 (2021), 123393.
[17] G. Kim, B. Yang, K. Cho, E. Kim, H.-K. Lee, Influences of CNT dispersion and pore characteristics on the electrical performance of cementitious composites, Composite Structures 164 (2017) 32–42.
[18] H. Cui, T.Y. Lo, S.A. Memon, F. Xing, X. Shi, Analytical model for compressive strength, elastic modulus and peak strain of structural lightweight aggregate concrete, Construction and Building Materials 36 (2012) 1036–1043.
[19] Y. Ren, Z. Yu, Q. Huang, Z. Ren, Constitutive model and failure criterions for lightweight aggregate concrete: A true triaxial experimental test, Construction and Building Materials 171 (2018) 759–769.
[20] J.Y. Yoon, H. Kim, Y.-J. Lee, S.-H. Sim, Prediction model for mechanical properties of lightweight aggregate concrete using artificial neural network, Materials 12 (17) (2019) 2678.
[21] A.J. Tenza-Abril, Y. Villacampa, A.M. Solak, F. Baeza-Brotons, Prediction and sensitivity analysis of compressive strength in segregated lightweight concrete based on artificial neural network using ultrasonic pulse velocity, Construction and Building Materials 189 (2018) 1173–1183.
[22] B. Yang, J.-U. Jang, S.-H. Eem, S.Y. Kim, A probabilistic micromechanical modeling for electrical properties of nanocomposites with multi-walled carbon nanotube morphology, Composites Part A: Applied Science and Manufacturing 92 (2017) 108–117.
[23] R. Wong, K.T. Chau, Estimation of air void and aggregate spatial distributions in concrete under uniaxial compression using computer tomography scanning, Cement and Concrete Research 35 (8) (2005) 1566–1576.
[24] R. Kumar, B. Bhattacharjee, Porosity, pore size distribution and in situ strength of concrete, Cement and concrete research 33 (1) (2003) 155–164.
[25] W. Ren, Z. Yang, R. Sharma, C. Zhang, P.J. Withers, Two-dimensional X-ray CT image based meso-scale fracture modelling of concrete, Engineering Fracture Mechanics 133 (2015) 24–39.
[26] A. Pouya, A finite element method for modeling coupled flow and deformation in porous fractured media, International Journal for Numerical and Analytical Methods in Geomechanics 39 (16) (2015) 1836–1852.

[27] H.-K. Lee, J. Ju, 3D micromechanics and effective moduli for brittle composites with randomly located interacting microcracks and inclusions, International Journal of Damage Mechanics 17 (5) (2008) 377–417.
[28] J. Ju, K. Yanase, Micromechanics and effective elastic moduli of particle-reinforced composites with near-field particle interactions, Acta Mechanica 215 (1) (2010) 135–153.
[29] B. Yang, B. Kim, H.-K. Lee, Micromechanics-based viscoelastic damage model for particle-reinforced polymeric composites, Acta Mechanica 223 (6) (2012) 1307–1321.
[30] J. Ju, H.-K. Lee, A micromechanical damage model for effective elastoplastic behavior of ductile matrix composites considering evolutionary complete particle debonding, Computer Methods in Applied Mechanics and Engineering 183 (3–4) (2000) 201–222.
[31] B. Yang, H. Shin, H.-K. Lee, H. Kim, A combined molecular dynamics/micromechanics/finite element approach for multiscale constitutive modeling of nanocomposites with interface effects, Applied Physics Letters 103 (24) (2013), 241903.
[32] B. Karihaloo, D. Fu, A damage-based constitutive law for plain concrete in tension, European journal of mechanics. A. Solids 8 (5) (1989) 373–384.
[33] Z. Liang, H.-K. Lee, W. Suaris, Micromechanics-based constitutive modeling for unidirectional laminated composites, International journal of solids and structures 43 (18–19) (2006) 5674–5689.
[34] H.-K. Lee, S. Pyo, 3D-damage model for fiber-reinforced brittle composites with microcracks and imperfect interfaces, Journal of engineering mechanics 135 (10) (2009) 1108–1118.
[35] J. Ju, T.M. Chen, Micromechanics and effective moduli of elastic composites containing randomly dispersed ellipsoidal inhomogeneities, Acta Mechanica 103 (1) (1994) 103–121.
[36] S.Y. Kim, J.-U. Jang, B.F. Haile, M.W. Lee, B. Yang, Swarm intelligence integrated micromechanical model to investigate thermal conductivity of multi-walled carbon nanotube-embedded cyclic butylene terephthalate thermoplastic nanocomposites, Composites Part A: Applied Science and Manufacturing 128 (2020), 105646.
[37] A.S. Fraser, Simulation of genetic systems by automatic digital computers I, Introduction, Australian journal of biological sciences 10 (4) (1957) 484–491.
[38] R.C. Eberhart, Y. Shi, Computational Intelligence: Concepts to Implementations, Elsevier, 2011.
[39] H. Jeon, J. Yu, H. Lee, G. Kim, J.W. Kim, Y.C. Jung, C.-M. Yang, B. Yang, A combined analytical formulation and genetic algorithm to analyze the nonlinear damage responses of continuous fiber toughened composites, Computational Mechanics 60 (3) (2017) 393–408.
[40] M. Shakouri, Analytical solution for stability analysis of joined cross-ply thin laminated conical shells under axial compression, Composite Materials and Engineering 3 (2) (2021) 117–134.
[41] V. Khonsari, E. Eslami, A. Anvari, Effects of expanded perlite aggregate (EPA) on the mechanical behavior of lightweight concrete, Proceedings of the 7th International Conference on Fracture and Mechanics of Concrete & Concrete Structure (FraMCoS-7), Jeju, Korea, 2010, pp. 1354-1361.
[42] M. Tafesse, R.-H. Kim, B. Yang, H.-K. Kim, Mix Proportioning of Concrete Containing Brick Chips as Coarse Aggregate for Cost Minimization, Magazine of the Korea Concrete Institute 32 (6) (2020) 583–592.